A Self-Powered Synchronous Switch Energy Extraction Circuit for Electromagnetic Energy Harvesting Enhancement

Zhiwu Xie, Li Teng, *Student Member, IEEE*, Haoyu Wang, *Senior Member, IEEE*, Yu Liu, *Senior Member, IEEE*, Minfan Fu, *Senior Member, IEEE*, and Junrui Liang, *Senior Member, IEEE*

***Abstract*—Previous studies have shown that the synchronous switch energy extraction (SSEE) solutions could enhance the energy harvesting capability of vibration energy harvesters with capacitive output impedance, such as piezoelectric ones. These circuits use a synchronous switch inductive branch to compensate for the capacitive source. Some studies have also shown that an inductive source can be compensated by a synchronous switch capacitive branch. Yet, the controls were all carried out by external bulky and power-hungry controllers, which is unrealistic in a self-contained and self-sustainable system. This article proposes a self-powered SSEE (SP-SSEE) circuit for inductive electromagnetic energy harvesting sources. The sampling, synchronization, and switch control are implemented with a small series sampling inductor, a comparator, and some digital gates, respectively. The SSEE circuit carries out two rounds of the switch ON/OFF actions in each vibration cycle to make the current through the induced equivalent voltage source in phase with its voltage. By improving the power factor of the induced voltage source, it enlarges the harvested power under the same excitation. It uses fewer switching actions than the conventional pulse-width modulation ac–dc rectifier designs. Moreover, the self-powered design makes the SSEE solution a passive ac–dc rectifier, which is more convenient to be utilized in real applications. The detailed working principle and experimental validation of the SP-SSEE circuit are provided in this article. The results show that, under the tested frequencies, SP-SSEE outperforms the benchmark standard energy harvesting diode-bridge rectifier by 62.1%–96.4% under different excitation frequencies, in terms of harvested power.**

***Index Terms*—Electromagnetic energy harvesting (EMEH), self-powered design, synchronous switch interface circuit.**

I. Introduction

THE Internet of Things (IoT) technology has grown rapidly in recent years. There will be numerous wireless sensor networks (WSNs) deployed in our surroundings in the future [1]. One of the factors confining the distribution range and operation life of WSN is sustainable power supply [2]. The working time of conventional battery-based WSN devices is limited by the capacity of chemical batteries [3]. Energy harvesting (EH) technology is a promising power solution to relieve the dependence on batteries. It explores how to scavenge energy in different physical forms from the environment and convert it into useful electricity, such that to provide autonomous power to WSNs. With the development of EH technology, battery dependency can be alleviated. More WSNs are expected to become self-powered in the coming future [4], [5], [6].

The electromagnetic (EM) transducer, sometimes just called a generator, is one of the most classical and widely used electromechanical transducers for kinetic energy harvesting [7]. A simplified EM generator and its equivalent electrical model are shown in Fig. 1. An EM generator can be modeled as an ac voltage source in series with the coil's self-inductance and resistance. The physical phenomenon was modeled with the well-known Faraday's law of induction. When the magnetic flux through the coil changes, an electromotive force can be induced within the coil.

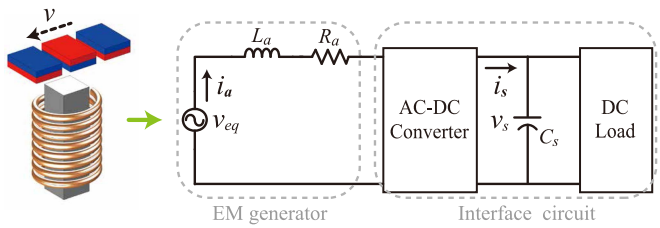

Fig. 1. Block diagram of an EMEH system.

A. Existing PWM-Based Electromagnetic Energy Harvesting (EMEH) Interface Circuits

To use the generated power for powering the digital electronics, an ac–dc rectifier and a dc–dc regulator are usually needed for power conditioning [8]. The configuration of an EM generator with the ac–dc interface circuit is shown in Fig. 1. The interface circuit plays an essential role in EMEH enhancement. Many studies have discussed the EMEH interface circuit designs during the last decade. From the simplest diode-bridge

Manuscript received 10 October 2022; revised 19 February 2023 and 5 April 2023; accepted 28 April 2023. Date of publication 3 May 2023; date of current version 21 June 2023. This work was supported in part by the Natural Science Foundation of Shanghai under Grant 21ZR1442300 and in part by the National Natural Science Foundation of China under Grants 62271319 and U21B2002. Recommended for publication by Associate Editor K. A. Kim. *(Corresponding author: Junrui Liang.)*

The authors are with the School of Information Science and Technology, ShanghaiTech University, Shanghai 201210, China, and also with the Shanghai Engineering Research Center of Energy Efficient and Custom AI IC, Shanghai 201210, China (e-mail: xiezhw@shanghaitech.edu.cn; tengli@shanghaitech.edu.cn; wanghy@shanghaitech.edu.cn; liuyu@shang-haitech.edu.cn; fumf@shanghaitech.edu.cn; liangjr@shanghaitech.edu.cn).

Color versions of one or more figures in this article are available at https://doi.org/10.1109/TPEL.2023.3272586.

Digital Object Identifier 10.1109/TPEL.2023.3272586

rectifier as a standard energy harvesting (SEH) circuit [9] to the converters using active controls, such as those driven by pulse-width modulation (PWM) [10] or pulse frequency modulation control [11] strategies. The SEH interface is passive and easy to be implemented for full-wave rectification; therefore, it was extensively applied in most EH from ac sources, such as EMEH and piezoelectric energy harvesting (PEH). Yet, due to the relatively considerable forward voltage drop of diodes when compared with the magnitude of the induction voltage, the low-voltage ac output generated by most EMEH generators can hardly go across the SEH interface circuit. Much harvested power is dissipated in the bridge rectifier. Some studies removed the diode bridge passive rectifier and proposed the actively controlled single-stage full-wave rectifiers [12]. In these designs, the passive rectifier is replaced by an active rectifier derived from typical dc–dc converter topologies. Additional components or modules are needed for sensing the polarity of v_{eq}, according to which the correct switching control sequence can be carried out. An alternative solution without using polarity identification is to use a dual boost ac–dc converter [13], [14], [15]. These converters utilize a bidirectional switch to deal with the positive or negative input voltage in each half cycle; therefore, they can realize voltage magnification under any polarity. Moreover, for the low-power EMEH system, maximizing the harvested power as much as possible makes it more feasible to better power IoT embedded systems. Maximum power transfer can be achieved when the equivalent impedance of a power converter matches that of the source impedance of an EM generator [16]. Most of the aforementioned designs have excluded the energy and effort in control implementation. These designs were derived from the PWM converter, which operates under high switching frequencies, say, up to several kHz. As the switching frequency is much higher than that of the voltage source, the switching loss and driver loss may account for a significant portion of the generated power, or even be unable to make ends meet. The self-powered switch driver and controller were not realized in many EMEH interface circuits. Without considering the issue of self-powered implementation, a self-contained and self-sustainable application will never be realized.

B. Synchronous Switch Interface Circuits

The synchronous switch interface circuits were well-studied and utilized to enhance the harvesting capability in PEH, a counterpart of EMEH. The most significant difference between EM and piezoelectric sources, in terms of electrical characteristics, is that an EM source is an inductive source, while a piezoelectric source is a capacitive one. In PEH, when the fundamental SEH interface circuit is used, due to the capacitive source impedance, there is a phase lag between the piezoelectric voltage and the internal equivalent current source. As we can observe from Fig. 2(a), the phase lag introduces negative power from the equivalent current source, i.e., in a short interval, some energy returns to the source. To eliminate the negative power, the synchronous switch technique is developed to make the voltage follow the polarity of the equivalent current. For instance, the EH capability can be significantly enhanced to

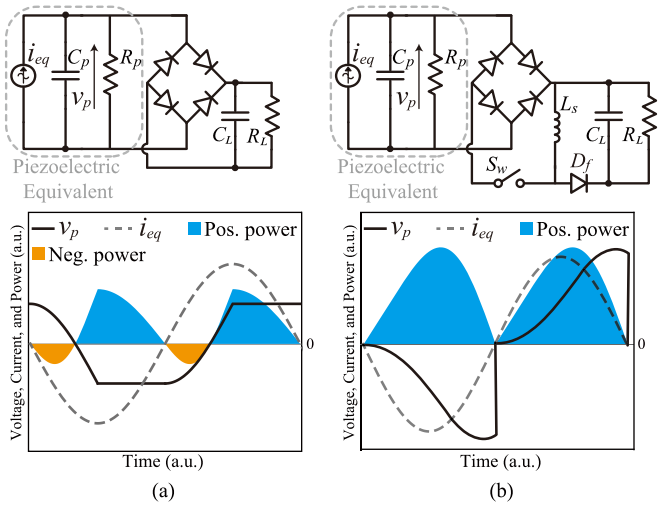

Fig. 2. Principle of synchronous switch interface circuit in PEH, a counterpart of EMEH generator. (a) Benchmark SEH circuit. (b) SECE circuit.

four folds of the optimal SEH case under weakly coupling conditions by taking the synchronized electric charge extraction (SECE) solution [17], [18], [19]. The circuit topology and typical waveform of SECE are shown in Fig. 2(b). The working process of SECE is summarized as follows. The piezoelectric source is open circuit in most of a vibration cycle, in which the equivalent current source i_{eq} charges the piezoelectric capacitance C_p. In the meanwhile, a small amount of energy is dissipated in the dielectric resistance R_p. At the zero-crossing point (ZCP) of i_{eq}, the switch S_w turns on for a quarter of an LC cycle. With the transient RLC response, the energy stored in C_p will be transferred to the inductor L_s. When C_p is fully discharged, S_w turns OFF. The energy absorbed by the inductor L_s will be released to the storage or load through the freewheeling (FW) diode D_f. The switch S_w only switches ON/OFF twice in each vibration cycle. As we can see from the SECE waveform, the piezoelectric voltage v_p and equivalent current source i_{eq} have the same polarity after taking the synchronous switch actions. The power from the i_{eq} source not only becomes always positive but also increases significantly, as shown by the cyan area in Fig. 2(b).

An EM source has a reciprocal equivalent internal structure to the piezoelectric one, say, a current source in parallel with a capacitance in the piezoelectric case becomes a voltage source in series with an inductance in the EM source. Negative power in some intervals is also observed when using the simplest SEH interface circuit [20]. The concept of the synchronous switch technique can be migrated from the PEH to the EMEH source by inserting a capacitive synchronous switch interface circuit for EMEH enhancement [21], [22], [23]. The improvement by using a synchronous switch circuit is more significant when the effect of the reactive component is more dominant over the resistive component in the internal source impedance, i.e., when an ac source has a larger quality factor. Therefore, the synchronous switch technique will be more useful when an EM generator operates at high speed [24], [25], [26], when its winding has

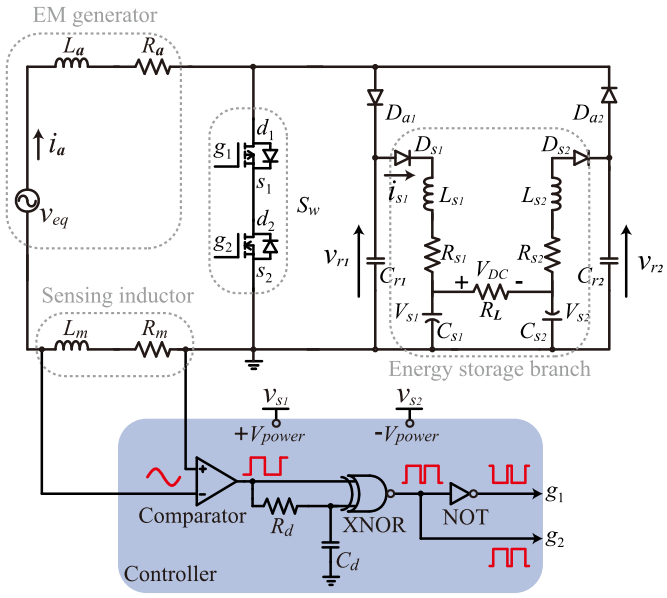

Fig. 3. Schematic of the proposed SP-SSEE circuit.

more turns, or when a winding core is made of high-permeability material [27], [28], [29].

Many self-powered synchronous switch circuits were developed for the PEH cases during the last decade [30], [31], [32], [33]. Yet, none was found for the EMEH case. All the implementations of existing synchronous switch interface circuits for EMEH used extra PC-based controllers [21], [22], [23], which are power hungry and bulky. For the first time, this article proposes a self-powered synchronous switch energy extraction (SP-SSEE) circuit for EMEH enhancement. Such a step from the energy-hungry implementation to the self-contained version facilitates the utilization of synchronous switch circuits in practical scenarios.

II. Working Principle

A. Topology

The schematic of the proposed SP-SSEE interface circuit is shown in Fig. 3. It consists of the equivalent model of an EM generator, sensing inductor, controller, two synchronous switch energy extraction (SSEE) circuit branches, and two FW and storage branches. The induced voltage v_{eq} is proportional to the relative velocity between the coil and the magnet. It is formulated as follows:

$$v_{\text{eq}}(t) = V_{\text{eq}} \sin(\omega t) \tag{1}$$

where, V_{eq} is the magnitude; ω is the vibration circular frequency. Synchronous switch actions are carried out when v_{eq} crosses zero, in order to instantaneously change i_a according to the polarity of v_{eq}. The switching branch for synchronous energy extraction (EE) is formed with a bidirectional switch S_w, which is composed of an N-channel and a P-channel MOSFETs, two diodes D_{ai} ($i = 1$ or 2), and two resonant capacitors C_{ri}. The series-connected C_{ri}, L_a, R_a, L_m, R_m, and D_{ai} form an underdamped RLC circuit to rapidly extract all energy in the inductance L_a and change the polarity of i_a at each synchronous instant. A FW and energy storage branch consists of a rectifier diode D_{si}, an inductor L_{si} (with parasitic resistance R_{si}), and an energy storage capacitor C_{si}. The capacitance of C_{si} is much greater than C_{ri}. The two storage capacitors C_{s1} and C_{s2} provide stable positive and negative voltage rails for powering the controller circuit. In the controller, a sensing inductor L_m is utilized to pick up the information of the current derivative. A comparator is used to identify the ZCP of the derivative, which is proportional to v_{eq}. An *RC* delay circuit and two logic gates generate the gate-drive pulses whenever a ZCP is detected. A dc load resistor R_L is connected across C_{s1} and C_{s2}.

B. Working Phases

The significant feature of SP-SSEE, compared with the conventional PWM-based design, is the low-frequency switch strategy, i.e., only two switch ON/OFF actions are needed in each vibration cycle. At the positive-to-negative ZCP of v_{eq}, it pumps energy from the EM inductance L_a to the positive storage capacitor C_{s1} through C_{r1}, and vice versa, to the negative storage capacitor C_{s2} through C_{r2} at the negative-to-positive ZCP of v_{eq}. Taking the former action, for example, the energy transfer process can be divided into four phases, short-circuit (SC), EE, charge transfer (CT), and FW phases. The conducting branches and typical waveform in the four phases are illustrated in Fig. 4.

1) SC Phase: The switch S_w is kept in on-state during the SC phase. The harmonically varying v_{eq} magnetizes the inductor L_a and L_m. The current i_a increases from zero, as shown in Fig. 4(b) and (c). The duration of this SC phase is about half of a vibration cycle.

2) EE Phase: When v_{eq} crosses zero from a positive value to a negative one, S_w is turned OFF for a short interval to enable a transient and rapid change of current i_a. The energy stored in the inductor L_a and L_m are extracted through the conducting branch highlighted in Fig. 4(d). Given the disturbance rejection of inductor current through L_{s1}, most of the transient current i_a flows through C_{r1}. Therefore, C_{r1} absorbs most of the energy extracted from inductors L_a and L_m. A little portion is dissipated because of joule heating in the parasitic resistance R_a, R_m, and diode D_{a1}. Neglecting the resonant branch containing L_{s1}, the conducting branching in the EE phase is an RLC circuit, which is formed by L_a, R_a, L_m, R_m, C_{r1}, and D_{a1}. At about a quarter of the *LC* period, which is much shorter than a vibration cycle, i_a drops to zero. The full-cycle and enlarged waveform is shown in Fig. 4(e) and (f). To completely demagnetize L_a and L_m, the turn-OFFinterval of S_w is slightly longer than a quarter of the *LC* period.

3) CT Phase: After the EE phase, S_w is turned ON again. The conducting branches are highlighted in Fig. 4(g). It starts the magnetization of L_a and L_m with negative v_{eq} in the next half vibration cycle. In the meanwhile, the extracted energy stored in C_{r1} is transferred to the energy storage branch. C_{s1} is sufficiently large; therefore, it can be regarded as a constant voltage source. C_{r1}, L_{s1}, and R_{s1} form an transient RLC circuit for the CT from C_{r1} to the storage C_{s1}. The corresponding waveform is shown in Fig. 4(h) and (i).

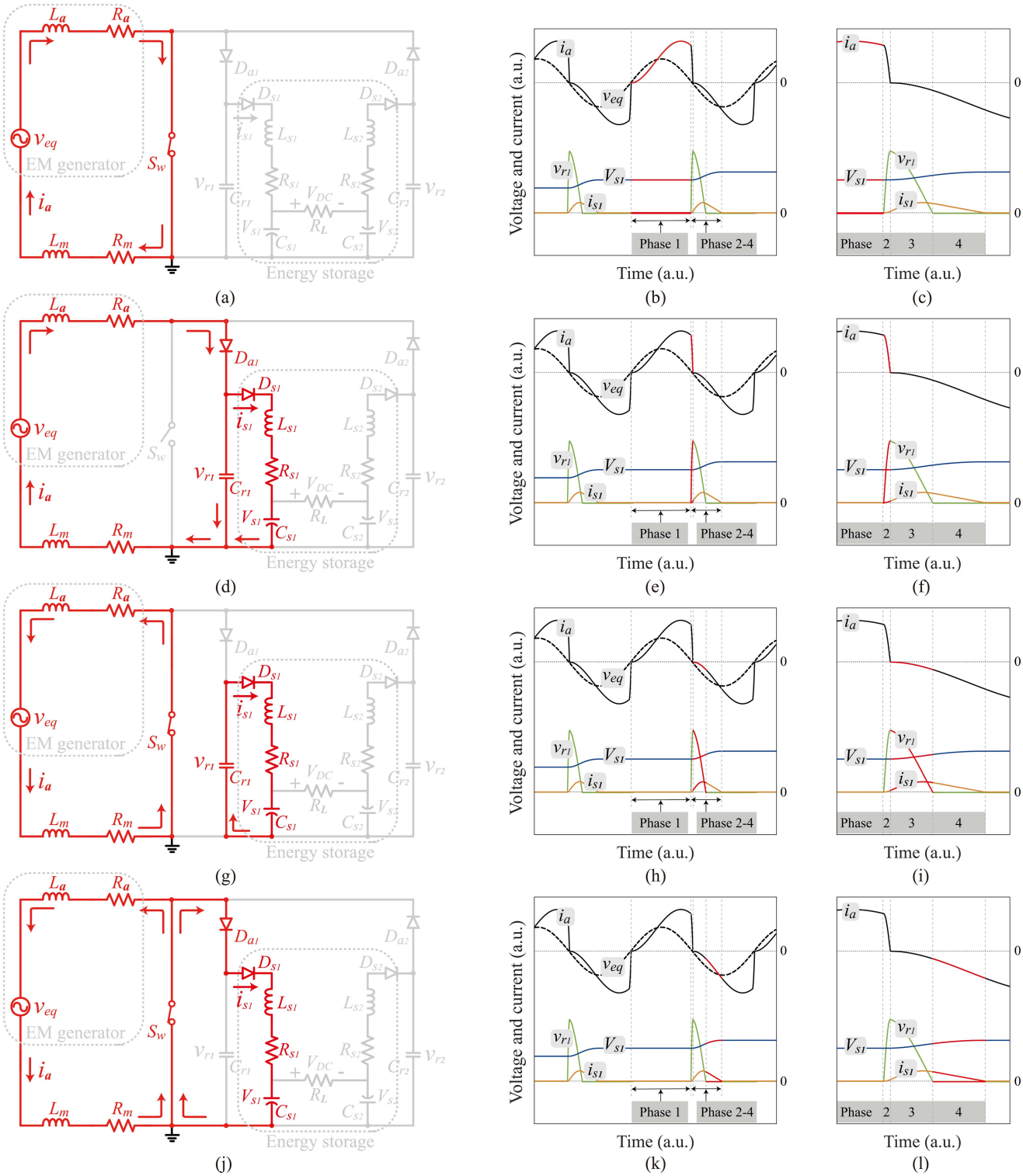

Fig. 4. Four working phases of SP-SSEE in the positive v_{eq} half vibration cycle. (a)–(c) SC phase. (d)–(f) EE phase. (g)–(i) CT phase. (j)–(l) FW phase. (a), (d), (g), and (j) Conducting circuit branch. (b), (e), (h), and (k) Operation waveform. (c), (f), (i), and (l) Enlarged views of EE, CT, and FW phases.

4) FW Phase: After C_{r1} is fully discharged, there is still some remaining energy in L_{s1}. It is further transferred to C_{s1} through the FW path formed by D_{a1}, D_{s1}, and S_w, as shown in Fig. 4(j). The major portion of extracted energy from L_a in this half-cycle finally arrives at the storage capacitance C_{s1}. Since L_a is only involved in the EE phase and C_{s1} only in the CT and FW phases, the transient energy source and load devices are decoupled in each synchronized switch action. Therefore, like SECE, its counterpart in PEH, the SSEE circuit decouples the EM source and the load.

C. ZCP Sensing

Accurately identifying the turn-OFF instants of the switch S_w is essential to perform the synchronous EE. These synchronous instants are at the ZCPs of the voltage source v_{eq}. However, v_{eq} is an equivalent element inside the EM generator, which cannot be separated. We need to add additional sensing elements to equivalently obtain the phase information of v_{eq}. In this article, we use an external inductor L_m for voltage sampling and ZCP identification. As shown in the conducting path of the SC phase in Fig. 4(a), L_m is connected in series with the EM generator. The EM current can be formulated as follows:

$$I_a(j\omega) = \frac{V_{\text{eq}}(j\omega)}{j\omega L_a + R_a + j\omega L_m + R_m + R_{ds(\text{on})}} \tag{2}$$

where, $R_{ds(\text{on})}$ is the total ON-resistance of S_w. The frequency-domain representation of voltage V_m across the inductor L_m can be derived as follows:

$$V_m(j\omega) = (j\omega L_m + R_m)\, I_a(j\omega). \tag{3}$$

To reflect the phase of v_{eq}, the inductance L_m and resistance R_m are designed to be much smaller than L_a and $R_a + R_{ds(\text{on})}$, respectively. Neglecting the $j\omega L_m$ and R_m terms, V_{eq} can be approximately taken as follows:

$$V_{\text{eq}}(j\omega) \approx \left[j\omega L_a + R_a + R_{ds(\text{on})}\right] I_a(j\omega). \tag{4}$$

Comparing (3) and (4), we can make the phase of v_m follow that of v_{eq} when selecting suitable values of L_m and R_m, which satisfy the proportional relation $L_m/R_m = L_a/[R_a + R_{ds(\text{on})}]$.

D. Control Unit

To autonomously control the switch in the self-powered synchronous switch circuit, a gate signal generator and a gate-drive circuit are needed. As shown in Fig. 4(f), in the EE phase, the switch S_w stays at the OFF state for a very short interval. An *RC* delay circuit and some logic gates are utilized to generate such a short pulse to switch OFF S_w during each synchronization instant. The control unit is shown in the controller part of Fig. 3. As the sensed v_m is in-phase with v_{eq}, their ZCPs can be identified by comparing the two nodal voltages across the sensing inductor. An analog comparator is utilized to carry out this zero-crossing detection. It converts the ZCP information to the rising or falling edges of the square-wave output signal. A digital XNOR gate turns the square-wave signal into the switch driving pulses. One of its input pins is connected to the comparator output; while the other is connected to the *RC* delay circuit. There is a phase difference between the edges of two digital input signals. Therefore, the XNOR generates a short pulse whenever a synchronized instant comes. The switch-OFF pulse duration should satisfy a lower bound, i.e., a quarter of an $(L_a + L_m)C_r$ cycle. For the upper bound, it is not that sensitive. The re-switch-ON instant affects the start point of the v_{eq} integral. Since v_{eq} is about zero in the vicinity, very fine tuning of R_d and C_d is not strictly required. The circuit works properly when the time constant R_dC_d is set to about one-third to one-half of the exactly required switch-OFF duration.

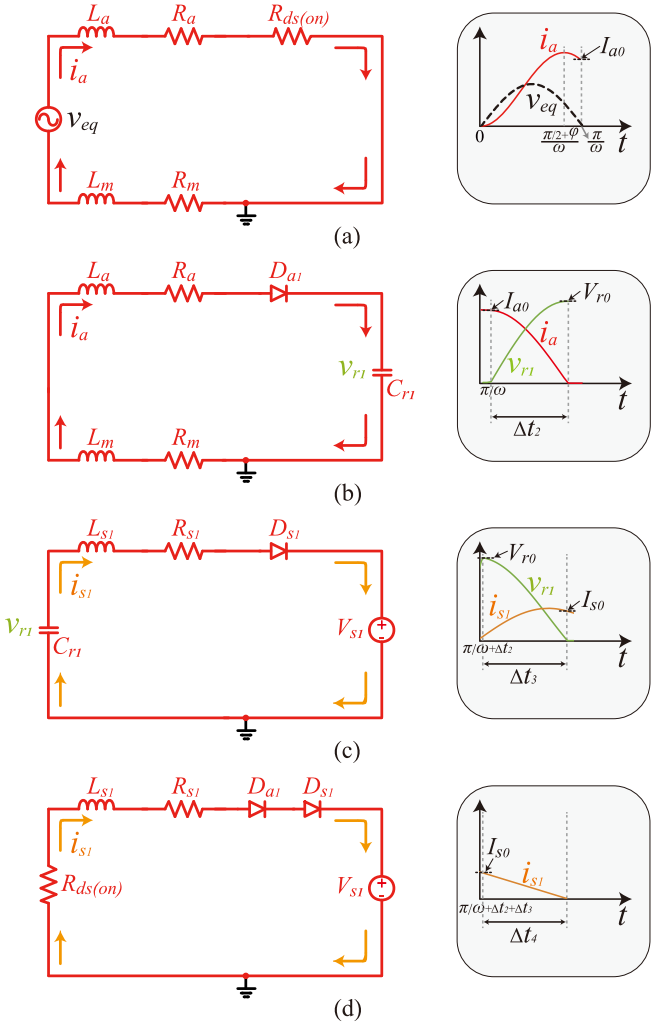

Fig. 5. Simplified equivalent conducting branches in four phases. (a) SC phase. (b) EE phase. (c) CT phase. (d) FW phase.

As introduced previously, the bidirectional switch S_w comprises a PMOS g_1 and an NMOS g_2. The XNOR output can be directly utilized to drive g_2. A NOT gate is utilized to generate a complementary driving voltage for g_1. All active components in the controller are powered by the SP-SSEE circuit itself. The positive and negative rails of the analog comparator and digital gates are connected to the outputs of the energy storage capacitor C_{s1} and C_{s2}, respectively.

III. Theoretical Analysis

Based on the working principle introduced in Section II, the dynamics of the conducting circuit branches in the four phases are theoretically analyzed in this section.

A. SC Phase

Fig. 5(a) shows the equivalent conducting path in the SC phase, in which inductors L_a and L_m are magnetized by v_{eq}. The current i_a can be formulated with a first-order differential

equation

$$v_{\text{eq}}(t) = L_1 \frac{\mathrm{d}i_a(t)}{\mathrm{d}t} + R_1 i_a(t) \tag{5}$$

where, $R_1 = R_a + R_m + R_{ds(\text{on})}$ and $L_1 = L_a + L_m$. The initial current of this phase is

$$i_a(0) = 0. \tag{6}$$

Solving (5) gives

$$i_a(t) = V_{\text{eq}} \frac{e^{-t/\tau} \sin\varphi + \sin(\omega t - \varphi)}{Z_1} \tag{7}$$

where, $\tau = L_1/R_1$ is the time constant of the first-order circuit; $\varphi = \sin^{-1}(\omega L_1/Z_1)$ represents the phase difference between v_{eq} and i_a; $Z_1 = \sqrt{(\omega L_1)^2 + R_1^2}$. The duration of this phase is approximately a half cycle of the voltage source v_{eq}. When this magnetizing process of the inductor L_a and L_m finished, the current i_a can reach

$$i_a\left(\frac{\pi}{\omega}\right) = I_{a0} = V_{\text{eq}} \frac{1 + e^{-\pi/(\omega\tau)}}{Z_1} \sin\varphi. \tag{8}$$

B. EE Phase

After the SC phase, the energy accumulated in the inductors L_a and L_m begins to release. Neglecting the small current flowing into the energy storage branch, the capacitor C_{r1}, inductors L_a and L_m, and diode D_{a1} form an RLC circuit, as shown in Fig. 5(b). It enables a rapid transient drop of i_a to zero. To simplify the expression of the result, we take the start time of this phase $t_2 = t - \pi/\omega$. The dynamics in this phase can be formulated with a second-order equation

$$L_1 C_{r1} \frac{\mathrm{d}^2 v_{r1}(t_2)}{\mathrm{d}t_2^2} + R_2 C_{r1} \frac{\mathrm{d}v_{r1}(t_2)}{\mathrm{d}t_2} + v_{r1}(t_2) + V_D = 0 \tag{9}$$

with the initial conditions of

$$C_{r1} \frac{\mathrm{d}v_{r1}(t_2)}{\mathrm{d}t_2}\bigg|_{t_2=0^+} = I_{a0}, \quad v_{r1}(0) = 0 \tag{10}$$

where, $R_2 = R_a + R_m$. V_D is the forward voltage drop of a diode. Solving (9), we have

$$v_{r1}(t_2) = \frac{e^{-\delta_1 t_2}}{\omega_1} \left[\frac{I_{a0}}{C_{r1}} \sin(\omega_1 t_2) + V_D \omega_{s1} \sin(\omega_1 t_2 + \beta_1)\right] - V_D. \tag{11}$$

In (11), the electrical damping ratio $\zeta_{s1} = 0.5 R_2 \sqrt{C_{r1}/L_1}$; the resonant angular frequency $\omega_{s1} = 1/\sqrt{L_1 C_{r1}}$. Other parameters are derived from ζ_{s1} and ω_{s1}, i.e., $\delta_1 = \omega_{s1}\zeta_{s1}$; $\omega_1 = \omega_{s1}\sqrt{1-\zeta_{s1}^2}$; $\beta_1 = \cos^{-1}(\delta_1/\omega_{s1})$.

During this phase, the energy stored in the inductor L_a and L_m is fully extracted. The current i_a drops to zero after an interval of

$$\Delta t_2 = \frac{1}{\omega_1} \cos^{-1}\left(\frac{C_{r1} V_D \omega_{s1} + I_{a0}\delta_1/\omega_{s1}}{\sqrt{C_{r1}^2 V_D^2 \omega_{s1}^2 + 2 C_{r1} V_D I_{a0} \delta_1 + I_{a0}^2}}\right). \tag{12}$$

The voltage across capacitor C_{r1} at the end of this EE phase, i.e., $V_{r0} = v_{r1}(\Delta t_2)$, can be derived by substituting (12) into (11).

C. CT Phase

When the EE phase is finished, the CT phase starts. C_{r1} begins to discharge through the energy storage branch. The corresponding equivalent circuit is shown in Fig. 5(c). As C_{s1} is designed much larger than C_{r1}, it can be regarded as a constant voltage source in each round of instantaneous charging. The dynamics of the equivalent circuit in the CT phase can be formulated with a second-order equation

$$L_{s1} C_{r1} \frac{\mathrm{d}^2 v_{r1}(t_3)}{\mathrm{d}t_3^2} + R_{s1} C_{r1} \frac{\mathrm{d}v_{r1}(t_3)}{\mathrm{d}t_3} + v_{r1}(t_3) - V_D - V_{s1} = 0 \tag{13}$$

where, $t_3 = t - \pi/\omega - \Delta t_2$. Given the initial conditions

$$\frac{\mathrm{d}v_{r1}(t_3)}{\mathrm{d}t_3}\bigg|_{t_3=\Delta t_3} = 0, \quad v_{r1}(0) = V_{r0} \tag{14}$$

by solving (13), we get

$$v_{r1}(t_3) = \frac{\omega_{s2}}{\omega_2}(V_{r0} - V_{s1} - V_D) e^{-\delta_2 t_3} \sin(\omega_2 t_3 + \beta_2) + V_D + V_{s1}. \tag{15}$$

In (15), the electrical damping ratio $\zeta_{s2} = 0.5 R_{s1}\sqrt{C_{r1}/L_{s1}}$; the resonant angular frequency $\omega_{s2} = 1/\sqrt{L_{s1} C_{r1}}$. Other parameters are derived from ζ_{s2} and ω_{s2}, i.e., $\delta_2 = \omega_{s2}\zeta_{s2}$; $\omega_2 = \omega_{s2}\sqrt{1-\zeta_{s2}^2}$; $\beta_2 = \cos^{-1}(\delta_2/\omega_{s2})$. The discharging current of C_{r1} can be derived from (15), i.e.,

$$i_{s1,\text{CT}}(t_3) = -C_{r1}\frac{\mathrm{d}v_{r1}(t_3)}{\mathrm{d}t_3} = C_{r1}\frac{\omega_{s2}^2}{\omega_2}(V_{r0} - V_{s1} - V_D) e^{-\delta_2 t_3} \sin(\omega_2 t_3). \tag{16}$$

At the end of the CT phase, the capacitor C_{r1} is fully discharged. The duration of the CT phase can be approximately obtained as follows:

$$\Delta t_3 \approx \frac{1}{\omega_2}\left[\pi - \beta_2 - \sin^{-1}\frac{-(V_{s1} + V_D)\omega_2}{(V_{r0} - V_D - V_{s1})\omega_{s2}}\right]. \tag{17}$$

The discharging current at the end of this CT phase, i.e., $I_{s0} = i_{s1,\text{CT}}(\Delta t_3)$, can be derived by substituting (17) into (16).

D. FW Phase

When the CT phase is finished, there is still some residual energy in the inductor L_{s1}. The inductor current i_{s1} freewheels through the bidirectional switch S_w. The equivalent circuit is shown in Fig. 5(d). The voltage across L_{s1} is clamped at $V_{s1} + 2V_D$. The current i_{s1} can be formulated with a first-order differential equation

$$L_{s1}\frac{\mathrm{d}i_{s1,\text{FW}}(t_4)}{\mathrm{d}t_4} + i_{s1,\text{FW}}(t_4) R_3 + 2V_D + V_{s1} = 0 \tag{18}$$

where, $t_4 = t - \pi/\omega - \Delta t_2 - \Delta t_3$ and $R_3 = R_{ds(\text{on})} + R_{s1}$. Given the initial condition

$$i_{s1,\text{FW}}(0) = I_{s0} \tag{19}$$

by solving (18), we get

$$i_{s1,\text{FW}}(t_4) = I_{s0} e^{-\frac{R_3}{L_{s1}} t_4} + \frac{V_{s1} + 2V_D}{R_3} \left(e^{-\frac{R_3}{L_{s1}} t_4} - 1 \right). \tag{20}$$

After this phase, the inductor current i_{s1} drops to zero, i.e., $i_{s1,\text{FW}}(\Delta t_4) = 0$. The duration Δt_4 can be derived as follows:

$$\Delta t_4 = -\frac{L_{s1}}{R_3} \ln \frac{V_{s1} + 2V_D}{I_{s0} R_3 + V_{s1} + 2V_D}. \tag{21}$$

E. Harvested Power

The harvested power is an important index evaluating the EH capability under the same mechanical excitation. As illustrated in Fig. 5, within the four working phases of the positive v_{eq} half cycle, the storage capacitor C_{s1} absorbs energy only in the CT and FW phases. In the other negative v_{eq} half cycle, C_{s2} harvests the same amount of energy with the complementary circuit branches. Thus, the average harvested power is formulated as follows:

$$P_h = \frac{\omega V_{s1}}{\pi} \left[\int_0^{\Delta t_3} i_{s1,\text{CT}}(t_3) \mathrm{d}t_3 + \int_0^{\Delta t_4} i_{s1,\text{FW}}(t_4) \mathrm{d}t_4 \right]. \tag{22}$$

The theoretical results can be obtained by numerically calculating the integrals in (22).

It should be noted that the energy consumption of the controller is not included in this theoretical analysis. It is strongly determined by the selected components and IC chips. In practical implementation, we should carefully choose the controller elements to minimize consumption as much as possible.

IV. Experiments and Results

Circuit simulation and experiment are carried out to validate the proposed SP-SSEE circuit and evaluate its performance. The simulation is built and runs in PSIM (Powersim Inc.) circuit simulator. The experimental setup includes an EM generator and a printed circuit board prototype, as shown in Fig. 6. The main structure of the EM generator is composed of a circular permanent magnet (PM) array and a copper coil wound on a magnetic core. The PM array rotor is driven by a motor. The amplitude and frequency of the equivalent voltage source v_{eq} can be adjusted by tuning the motor speed. As explained in Section I-B, the effectiveness of the SP-SSEE circuit is significant for an inductive EM generator, i.e., its internal impedance is inductive and the inductive component ωL_a is larger than or comparable to the resistive component R_a. There are two methods to increase ωL_a: a) to increase the frequency f of the voltage source v_{eq}; b) to increase the self-inductance L_a. In this design, we use both methods to increase ωL_a. To increase the self-inductance, the coil is wound on a magnetic core with high permeability. To increase the source frequency, the number of magnet pairs and the rotating speed should be increased in the

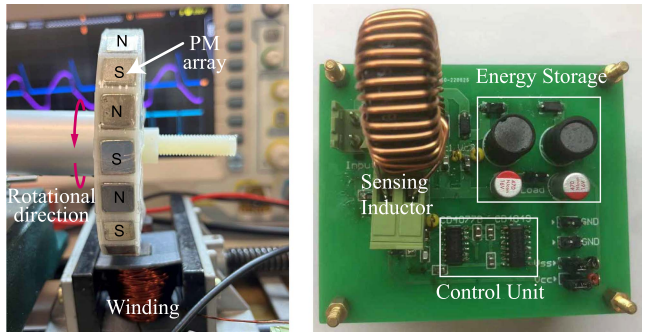

EM Generator SP-SSEE Circuit

Fig. 6. Experimental setup.

TABLE I
Circuit Parameters

Component/Part	Value/Type
Self-inductance L_a, self-resistance R_a	4.4 mH, 1.4 Ω
Sensing inductance L_m, resistance R_m	200 μH, 60 mΩ
Inductance L_{s1}, L_{s2}, resistance R_{s1}, R_{s2}	47 mH, 52 Ω
NMOS g_2, on-resistance	VBA5415, 18 mΩ
PMOS g_1, on-resistance	VBA5415, 22 mΩ
Diode forward voltage V_D	0.5 V
Analog comparator	TLV3701
NOT gate, XNOR gate	CD4049, CD4077
Delay resistance R_d, capacitor C_d	100 kΩ, 1 nF
Energy storage capacitor C_{s1}, C_{s2}	470 μF
Resonant capacitor C_{r1}, C_{r2}	2 μF
Phase durations Δt_2, Δt_3	0.148 ms, 0.62 ms
Phase duration Δt_4	0.53 ms

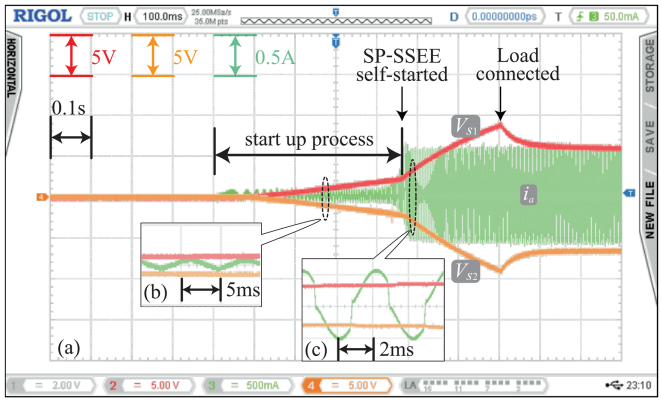

Fig. 7. SP-SSEE waveform from startup to steady-state operation. ($V_{\text{eq}} = 3.5$ V; $f = 260$ Hz). (a) Overview of storage voltages V_{s1}, $V_{s,2}$, and current i_a. (b) Enlarged view in the startup process. (c) Enlarged view in steady-state operation.

design and operation processes, respectively. As a result, the self-inductance L_a and R_a are obtained to be approximately 4.4 mH and 1.4 Ω, respectively. All parameters of the SP-SSEE circuit are listed in Table I.

In the first experiment, the amplitude and frequency of v_{eq} are set to $V_{\text{eq}} = 3.5$ V and $f = 260$ Hz, respectively. The experiment waveform of the SP-SSEE circuit from start-up to normal steady-state operation process is shown in Fig. 7. In the startup process, the diode-bridge rectifier passively charges the capacitors C_{s1} and C_{s2}. The cold start bridge is formed by the

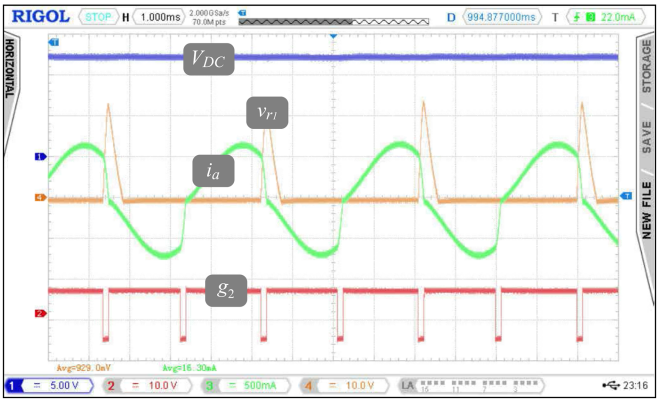

Fig. 8. Steady-state waveform showing more transient operation details ($V_{\text{eq}} = 3.5$ V; $f = 260$ Hz).

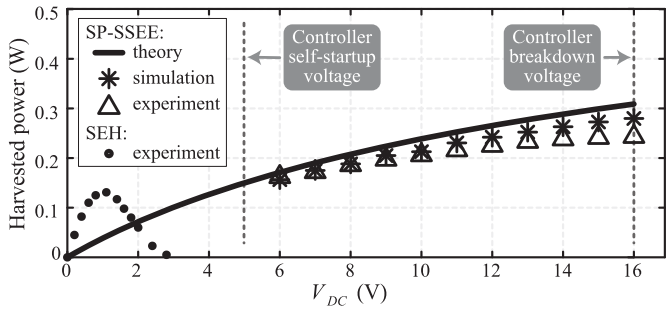

Fig. 9. Harvested power results of the prototyped EMEH using SP-SSEE under different dc load voltages ($V_{\text{eq}} = 3.5$ V, $f = 260$ Hz).

diodes D_{a1}, D_{s1}, D_{a2}, and D_{s2}. After the voltages across C_{s1} and C_{s2} reach the control unit's minimum operating threshold voltage V_t (resulting from the supply voltage requirements of the analog comparator and digital gates), the SP-SSEE circuit starts to operate. Thus, to activate the SP-SSEE circuit, the peak value of the transducer minimum output voltage should be greater than $V_t + 2V_D$, which is about 5 V in this study. From the waveform shown in Fig. 7, the charging speed of C_{s1} and C_{s2} is significantly improved after the activation of SSEE. The storage voltages approach the steady state sometime after the load connection, which is done manually in this experiment. The steady-state waveform of the SP-SSEE circuit is recorded and shown in Fig. 8. It can be observed that the EM current i_a in green can rapidly drop to zero every time after a short turn-OFF interval of switch S_w. The experimental waveform shows a good agreement with the conceptual one, which was illustrated in Fig. 4.

In the second experiment, under the same excitation ($V_{\text{eq}} = 3.5$ V and $f = 260$ Hz), the harvested power of the SP-SSEE circuit under different dc load voltages is investigated. Load resistors R_L with different values are connected across C_{s1} and C_{s2} in succession to draw different V_{dc}. The corresponding harvested power is indirectly obtained according to Joule's law $P_h = V_{\text{dc}}^2/R_L$. The theoretical, simulation, and experimental results of SP-SSEE, together with the experimental result of the diode bridge SEH circuit as a benchmark control, are shown in Fig. 9. In general, the theory, simulation, and experiment show a good agreement that SP-SSEE outperforms SEH almost one-fold when comparing their maximum harvested power. As we can see from the results of harvested power, there are some small gaps among the theoretical, simulation, and experimental results. These differences might be due to the power consumption of the controller and switch drive circuit, which was not considered in the theoretical derivation. Since this consumption might differ according to different selected components, it is unable to be accurately estimated in theory. The power dissipation of the parasitic resistances cannot be directly measured in the experiment either. We study the power dissipation breakdown with circuit simulation. The results are listed in Table II. From the results, R_a equivalent series resistance (ESR) of the coil and R_{s1} and R_{s2} ESR of the FW inductors L_{s1} and L_{s2} account for about 85% of the dissipated power.

TABLE II
POWER DISSIPATION BREAKDOWN IN SIMULATION

Component	Percentage	Power (mW)
Parasitic resistance R_a	40.2%	413
Parasitic resistance R_{s1} and R_{s2}	43.1%	442
Diodes D_{a1}, D_{a2}, D_{s1}, and D_{s2}	12.7%	130
Parasitic resistance R_m	2.3%	24
Switch on-resistance $R_{ds(on)}$	1.2%	12
Controller (in experiment)	0.5%	5

Simulation conditions: $V_{eq} = 3.5$ V; $f = 260$ Hz; $V_{DC} = 12$ V.

TABLE III
EH ENHANCEMENT IN THE EXPERIMENT

Frequency	P_h ratio*	Frequency	P_h ratio*
200 Hz	162.1%	280 Hz	187.4%
220 Hz	172.7%	300 Hz	191.7%
240 Hz	180.1%	320 Hz	194%
260 Hz	184.1%	340 Hz	196.4%

* P_h ratio $= \max(P_{h,\text{SP-SSEE}})/\max(P_{h,\text{SEH}}) \times 100\%$.

In the third experiment, we compare the maximum harvested power of SP-SSEE and that of the benchmark SEH circuit under different source frequencies. From the ratios of harvested power, which are summarized in Table III, we can find that the ratio of enhancement increases with the increase of source frequency. It shows good concordance with the argument that a larger inductive component in the source impedance gives better EH enhancement when using SP-SSEE. The ac sources with strong reactive impedance are the preference for manifesting the potential of SSEE technology toward EH enhancement.

V. DISCUSSION

A. Analogy to SECE in PEH

As shown in Fig. 8, the profiles of the current i_a and voltage v_{eq} waveform when using SSEE in EMEH look very similar to that of the piezoelectric voltage and equivalent current waveform when using SECE in PEH. It again demonstrates the reciprocal relation between the capacitive piezoelectric source

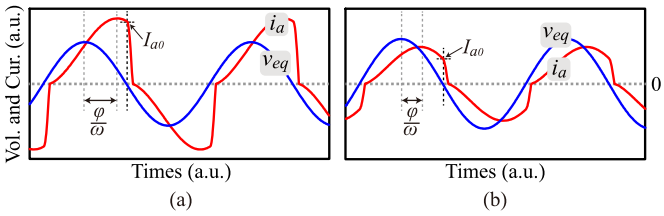

Fig. 10. Operating waveform of SP-SSEE in simulation under different Q values of the EM source. (a) $Q = 5.1$ (this prototype). (b) $Q = 1.2$.

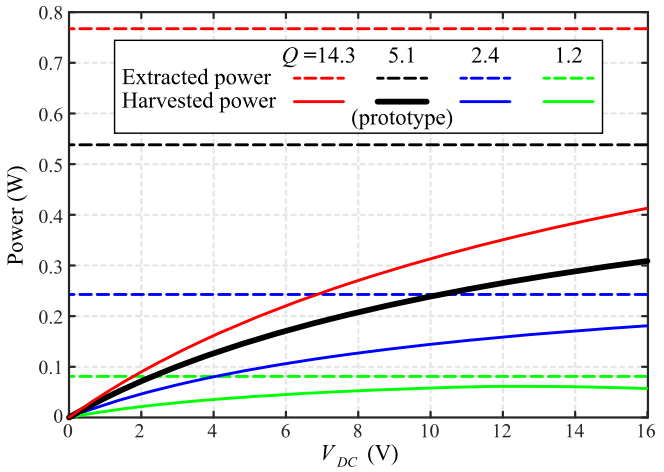

Fig. 11. Theoretical extracted power and harvested power under different quality factor Q of an EMEH source ($V_{\text{eq}} = 3.5$ V; $f = 260$ Hz).

and the inductive EM source, as well as that between their EH interface circuits and switch control schemes. When considering the synchronized switch solutions for an EM harvester, more experiences can be learned from its PEH counterpart.

B. Effect of Finite Quality Factor of an EMEH Source

As mentioned, a small quality factor or equivalently a dominant resistive component in the EM source is detrimental to the improvement of EH capability. In the SP-SSEE circuit working process, the switch S_w turns OFF at the ZCP of the voltage source v_{eq} to make the current i_a quickly drop to zero. When the source Q value decreases from an infinite number to a finite and smaller number, the phase lag between SC current i_a and equivalent voltage v_{eq} reduces from $\pi/2$ toward zero. The current i_a value at the synchronous switch instant, which is denoted as I_{a0}, decreases under a smaller Q condition, as shown in Fig. 10. It has a direct effect of reducing the extracted power, which is formulated as follows:

$$P_E = f(L_a + L_m)I_{a0}^2. \tag{23}$$

Fig. 11 illustrates the theoretical extracted power (dashed lines) under four different Q values. Because extraction is independent of the loading condition in SSEE, the extracted power is constant under different output voltages. In general, the SP-SSEE circuit is valuable to be applied for the more inductive EM sources.

TABLE IV
QUALITATIVE COMPARISON OF EMEH CIRCUITS

EMEH circuit	PWM-based [8]–[16]	SSEE
Switching frequency	High	Low
Control complexity	High	Low
Overall cost	High	Medium
Targeted EM generators	Inductive or resistive	Inductive
Self-powered implementation	Hard	Easy

C. Effect of Dissipation in the Switching Transient

Not all the extracted power is able to be harvested into storable dc energy. A considerable part of the extracted energy is dissipated in the power conditioning process [34]. Like the SECE case in PEH, the dissipation is basically caused by the parasitic resistance of the current paths and the voltage drops of those current steering diodes. The percentage of dissipation caused by the former reason has no relationship to the output voltage V_{dc}; while that caused by the latter decreases as the V_{dc} gets larger [35]. The former corresponds to the inevitable gap between extracted power and asymptotic constant harvested power at large V_{dc} in Fig. 11. The latter explains the rising trend of the harvested power as V_{dc} gets larger approaching an asymptotic value, regardless of different Q values.

D. Comparison to Existing PWM-Based EMEH

Most of the previous EMEH interface circuits were developed based on the PWM principle [8], [9], [10], [11], [12], [13], [14], [15], [16]. The synchronous switch technology makes a difference by using the transient underdamped response. Table IV provides a qualitative comparison between the PWM-based technology and SSEE. With the self-powered implementation proposed in this article, the SSEE solution better suits standalone and self-contained EMEH applications.

VI. CONCLUSION

The synchronous switch technique was studied for the power enhancement of EH using piezoelectric transducers for over two decades. Related studies were rarely seen for those using more classical EM transducers. This article has proposed a SP-SSEE circuit for realizing a self-contained solution for EM-based EH enhancement. The circuit topology, working principle, transient phases, and harvested power were discussed and analyzed in detail. A good agreement was shown among the theoretical, simulation, and experimental results, in terms of steady-state waveform and harvested power. Compared with the benchmark diode bridge SEH interface circuit, the proposed SP-SSEE circuit can harvest up to two-fold energy, under the same mechanical excitation. Moreover, the harvested power is more reluctant to the load variation in SP-SSEE. The application preference of such an SSEE technique, in which its effects can be better manifested, was discussed. Those EM harvesters with higher quality factors, i.e., have more significant inductive internal impedances, are more beneficial by applying this SP-SSEE technique. Such

a preferred working condition of SP-SSEE is realized when the coil's parasitic resistance is small, self-inductance is large, or the EM harvester operates under high frequency.

REFERENCES

[1] D. Newell and M. Duffy, "Review of power conversion and energy management for low-power, low-voltage energy harvesting powered wireless sensors," *IEEE Trans. Power Electron.*, vol. 34, no. 10, pp. 9794–9805, Oct. 2019.

[2] J. Bito, R. Bahr, J. G. Hester, S. A. Nauroze, A. Georgiadis, and M. M. Tentzeris, "A novel solar and electromagnetic energy harvesting system with a 3-d printed package for energy efficient Internet-of-Things wireless sensors," *IEEE Trans. Microw. Theory Tech.*, vol. 65, no. 5, pp. 1831–1842, May 2017.

[3] Z. Gao, M. Chen, K. Liu, J. Zhao, Y. Li, and G. Wang, "An asynchronous AC-DC boost converter with event-driven voltage regulator and 94 low-frequency electromagnetic energy harvesting," *IEEE Trans. Circuits Syst. II- Exp. Briefs*, vol. 68, no. 7, pp. 2563–2567, Jul. 2021.

[4] H. Xiao, H. Peng, X. Liu, and H. Sun, "Fully self-powered inductorless electromagnetic vibration energy harvesting system using auxiliary coils for hysteresis current MPPT control," *IEEE Trans. Power Electron.*, vol. 37, no. 11, pp. 13192–13204, Nov. 2022.

[5] Z. J. Chew, Y. Kuang, and M. Zhu, "Self-powered and self-configurable active rectifier using low voltage controller for wide output range energy harvesters," *IEEE Trans. Power Electron.*, vol. 37, no. 9, pp. 11285–11295, Sep. 2022.

[6] Z. Long et al., "Self-powered SSDCI array interface for multiple piezoelectric energy harvesters," *IEEE Trans. Power Electron.*, vol. 36, no. 8, pp. 9093–9104, Aug. 2021.

[7] S.-W. Wang, Y.-W. Ke, P.-C. Huang, and P.-H. Hsieh, "Electromagnetic energy harvester interface design for wearable applications," *IEEE Trans. Circuits Syst. II- Exp. Briefs*, vol. 65, no. 5, pp. 667–671, May 2018.

[8] G. D. Szarka, S. G. Burrow, P. P. Proynov, and B. H. Stark, "Maximum power transfer tracking for ultralow-power electromagnetic energy harvesters," *IEEE Trans. Power Electron.*, vol. 29, no. 1, pp. 201–212, Jan. 2014.

[9] G. D. Szarka, B. H. Stark, and S. G. Burrow, "Review of power conditioning for kinetic energy harvesting systems," *IEEE Trans. Power Electron.*, vol. 27, no. 2, pp. 803–815, Feb. 2012.

[10] R. Dayal, S. Dwari, and L. Parsa, "A new design for vibration-based electromagnetic energy harvesting systems using coil inductance of microgenerator," *IEEE Trans. Ind. Appl.*, vol. 47, no. 2, pp. 820–830, Mar./Apr. 2011.

[11] Y. Rao and D. P. Arnold, "An input-powered vibrational energy harvesting interface circuit with zero standby power," *IEEE Trans. Power Electron.*, vol. 26, no. 12, pp. 3524–3533, Dec. 2011.

[12] G. D. Szarka, S. G. Burrow, and B. H. Stark, "Ultralow power, fully autonomous boost rectifier for electromagnetic energy harvesters," *IEEE Trans. Power Electron.*, vol. 28, no. 7, pp. 3353–3362, Jul. 2013.

[13] S. Dwari, R. Dayal, and L. Parsa, "A novel direct ac/dc converter for efficient low voltage energy harvesting," in *Proc. 34th Annu. Conf. IEEE Ind. Electron.*, 2008, pp. 484–488.

[14] M. Shousha, D. Dinulovic, M. Haug, T. Petrovic, and A. Mahgoub, "A power management system for electromagnetic energy harvesters in battery/batteryless applications," *IEEE Trans. Emerg. Sel. Topics Circuits Syst.*, vol. 8, no. 4, pp. 3644–3657, Dec. 2020.

[15] J. Chen, H. Peng, Z. Feng, and Y. Kang, "A GaN BCM AC–DC converter for sub-1 v electromagnetic energy harvesting with enhanced output power," *IEEE Trans. Power Electron.*, vol. 36, no. 8, pp. 9285–9299, Aug. 2021.

[16] L. Wang, H. Wang, M. Fu, Z. Xie, and J. Liang, "Three-port power electronic interface with decoupled voltage regulation and MPPT in electromagnetic energy harvesting systems," *IEEE Trans. Ind. Appl.*, vol. 58, no. 2, pp. 2144–2154, Mar./Apr. 2022.

[17] E. Lefeuvre, A. Badel, C. Richard, and D. Guyomar, "Piezoelectric energy harvesting device optimization by synchronous electric charge extraction," *J. Intell. Mater. Syst. Struct.*, vol. 16, no. 10, pp. 865–876, 2005.

[18] A. Shareef, W. L. Goh, S. Narasimalu, and Y. Gao, "A rectifier-less AC-DC interface circuit for ambient energy harvesting from low-voltage piezoelectric transducer array," *IEEE Trans. Power Electron.*, vol. 34, no. 2, pp. 1446–1457, Feb. 2019.

[19] H. Xia et al., "A self-powered S-SSHI and SECE hybrid rectifier for PE energy harvesters: Analysis and experiment," *IEEE Trans. Power Electron.*, vol. 36, no. 2, pp. 1680–1692, Feb. 2021.

[20] J. Liang, C. Ge, and Y.-C. Shu, "Impedance modeling of electromagnetic energy harvesting system using full-wave bridge rectifier," in *Proc. Act. Passive Smart Struct. Integr. Syst.*, 2017, Art. no. 101642N.

[21] E. Arroyo and A. Badel, "Electromagnetic vibration energy harvesting device optimization by synchronous energy extraction," *Sens. Actuator A-Phys.*, vol. 171, no. 2, pp. 266–273, 2011.

[22] E. Arroyo, A. Badel, and F. Formosa, "Energy harvesting from ambient vibrations: Electromagnetic device and synchronous extraction circuit," *J. Intell. Mater. Syst. Struct.*, vol. 24, no. 16, pp. 2023–2035, 2013.

[23] G. Lombardi and M. Lallart, "Synchronous electric charge and induced current extraction (SECICE): A unified nonlinear technique combining piezoelectric and electromagnetic harvesting," *Smart Mater. Struct.*, vol. 30, no. 2, 2021, Art. no. 025029.

[24] D. Dinulovic et al., "Dual-rotor electromagnetic-based energy harvesting system for smart home applications," *IEEE Trans. Magn.*, vol. 57, no. 2, pp. 1–5, Feb. 2021.

[25] K. H.-k. Tse and H. S.-h. Chung, "MPPT for electromagnetic energy harvesters having non-negligible output reactance operating under slow-varying conditions," *IEEE Trans. Power Electron.*, vol. 35, no. 7, pp. 7110–7122, Jul. 2020.

[26] L. Teng, Z. Xie, Y. Yu, and J. Liang, "Synchronous switch current reversion (SSCR) technique for motor braking enhancement," in *Proc. IEEE Energy Convers. Congr. Expo.*, 2022, pp. 1–5.

[27] X. Xing, G. M. Yang, M. Liu, J. Lou, O. Obi, and N. X. Sun, "High power density vibration energy harvester with high permeability magnetic material," *J. Appl. Phys.*, vol. 109, no. 7, 2011, Art. no. 07E514.

[28] H. Chiriac, M. Tibu, N. Lupu, I. Skorvanek, and T. A. Ovari, "Nanocrystalline ribbons for energy harvesting applications," *J. Appl. Phys.*, vol. 115, no. 17, 2014.

[29] M. Gao, L. Yi, and J. Moon, "Mathematical modeling and validation of saturating and clampable cascaded magnetics for magnetic energy harvesting," *IEEE Trans. Power Electron.*, vol. 38, no. 3, pp. 3455–3468, Mar. 2023.

[30] J. Liang and W. H. Liao, "Improved design and analysis of self-powered synchronized switch interface circuit for piezoelectric energy harvesting systems," *IEEE Trans. Ind. Electron.*, vol. 59, no. 4, pp. 1950–1960, Apr. 2012.

[31] M. Lallart and D. Guyomar, "An optimized self-powered switching circuit for non-linear energy harvesting with low voltage output," *Smart Mater. Struct.*, vol. 17, no. 3, May 2008, Art. no.. 035030.

[32] Z. Chen, Y. Xia, G. Shi, X. Wang, H. Xia, and Y. Ye, "Self-powered multi-input serial SSHI interface circuit with arbitrary phase difference for piezoelectric energy harvesting," *IEEE Trans. Power Electron.*, vol. 36, no. 8, pp. 9183–9192, Aug. 2021.

[33] G. Shi, Y. Xia, X. Wang, L. Qian, Y. Ye, and Q. Li, "An efficient self-powered piezoelectric energy harvesting CMOS interface circuit based on synchronous charge extraction technique," *IEEE Trans. Circuits Syst. I, Reg. Papers*, vol. 65, no. 2, pp. 804–817, Feb. 2018.

[34] J. Liang and W.-H. Liao, "Energy flow in piezoelectric energy harvesting systems," *Smart Mater. Struct.*, vol. 20, no. 1, Dec. 2010, Art. no. 015005.

[35] C. Chen, B. Zhao, and J. Liang, "Revisit of synchronized electric charge extraction (SECE) in piezoelectric energy harvesting by using impedance modeling," *Smart Mater. Struct.*, vol. 28, no. 10, 2019, Art. no. 105053.

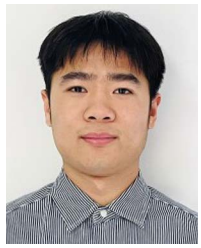

Zhiwu Xie received the B.E. degree in automation from Xiangtan University, Xiangtan, China, in 2016. He is currently working toward the master's degree with ShanghaiTech University, Shanghai, China.

His research interests include electromagnetic energy harvesting and power electronics.

Li Teng (Student Member, IEEE) received the B.S. degree in microelectronics from the Hefei University of Technology, Hefei, China, in 2015. He is currently working toward the Ph.D. degree with ShanghaiTech University, Shanghai, China.

From 2015 to 2016, he was an analog IC Design Engineer with Wuxi ETEK Microelectronics Company, Ltd, Wuxi, China. His research focuses on analog/mixed-signal IC design.

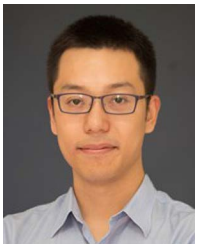

Haoyu Wang (Senior Member, IEEE) received the bachelor's degree (with Distinguished Hons.) in electrical engineering from Zhejiang University, Hangzhou, China, in 2009, and the Ph.D. degree in electrical engineering from the University of Maryland at College Park, College Park, MD, USA, in 2014.

In 2014, he joined the School of Information Science and Technology, ShanghaiTech University, Shanghai, China, where he is currently a Tenured Associate Professor. His research interests include power electronics, plug-in electric and hybrid electric vehicles, the applications of wide-bandgap semiconductors, renewable energy harvesting, and power management integrated circuits.

Dr. Wang is an Associate Editor for IEEE TRANSACTIONS ON INDUSTRIAL ELECTRONICS, IEEE TRANSACTIONS ON TRANSPORTATION ELECTRIFICATION, and *CPSS Transactions on Power Electronics and Applications*.

Yu Liu (Senior Member, IEEE) received the B.S. and M.S. degrees from Shanghai Jiao Tong University, Shanghai, China, in 2011 and 2013, respectively, and the Ph.D. degree from the Georgia Institute of Technology, Atlanta, GA, USA, in 2017, all in electrical engineering.

He is currently a Tenure-Track Assistant Professor with the School of Information Science and Technology, ShanghaiTech University, Shanghai, China. His research interests include modeling, protection, fault location, and state/parameter estimation of power systems and power electronic systems.

Minfan Fu (Senior Member, IEEE) received the B.S., M.S., and Ph.D. degrees in electrical and computer engineering from the University of Michigan—Shanghai Jiao Tong University Joint Institute, Shanghai Jiao Tong University, Shanghai, China, in 2010, 2013, and 2016, respectively.

From 2016 to 2018, he was a Postdoctoral Researcher with the Center for Power Electronics Systems, Virginia Polytechnic Institute, and State University, Blacksburg, VA, USA. He is currently an Assistant Professor with the School of Information Science and Technology, ShanghaiTech University, Shanghai, China. He holds one U.S. patent, and three Chinese patents, and has authored or coauthored more than 50 papers in prestigious IEEE journals and conferences. His research interests include megahertz wireless power transfer, high-frequency power conversion, high-frequency magnetic design, and the application of wide-bandgap devices.

Dr. Fu is currently an Associate Editor for the IEEE IES Industrial Electronics Technology News and the Section Chair of several conferences, such as IECON, IPEMC, and VEH. His conference paper for IECON 2019 won the IES-SYPA Competition. He is the Tutorial Speaker for IPEMC 2020 and ISIE 2020.

Junrui Liang (Senior Member, IEEE) received the B.E. and M.E. degrees in instrumentation engineering from Shanghai Jiao Tong University, Shanghai, China, in 2004 and 2007, respectively, and the Ph.D. degree in mechanical and automation engineering from The Chinese University Hong Kong, Hong Kong, in 2010.

He is currently an Associate Professor with the School of Information Science and Technology, ShanghaiTech University, Shanghai, China. His research interests include energy conversion and power conditioning circuits, kinetic energy harvesting and vibration suppression, IoT devices, and mechatronics.

Dr. Liang is an Associate Editor for *IET Circuits, Devices, and Systems* and the General Chair of the 2nd International Conference on Vibration and Energy Harvesting Applications (VEH) 2019. He was a recipient of five Best Paper Awards in international conferences, such as IEEE International Conference on Information and Automation 2009 and 2010, and International Conferences on Vibration and Energy Harvesting Applications 2021.